

Supplementary Information for Curvature-dependent propulsion of elastic flagella

Taylor E. Greenwood,^{a,b} Luis Felipe Córdoba,^{a,b} Jian Teng,^a Saebom Lee,^a Genevieve Dare,^c
Ebru Demir,^c On Shun Pak,^d and Yong Lin Kong^{*a,b}

^a Department of Mechanical Engineering, Rice University; Houston, TX, 77005 USA. Email: kong@rice.edu

^b Department of Mechanical Engineering, University of Utah; Salt Lake City, UT, 84112 USA

^c Department of Mechanical Engineering & Mechanics, Lehigh University; Bethlehem, PA, 18015 USA.

^d Department of Mechanical Engineering, Santa Clara University; Santa Clara, CA, 95053 USA.

I. SUPPORTING INFORMATION

A. In-plane actuation assumption

The flagellum's rectangular cross-section is designed with a $h:w$ (h is the flagellum height and w is the flagellum width, see Figure 1B) ratio of 10:1 to limit out-of-plane bending. This $h:w$ ratio was chosen based on the ratio of in-plane to out-of-plane deflection of a cantilever beam under a distributed load. The maximum deflection of a straight cantilever beam under a distributed load is $\delta_{max} = \frac{PL^4}{8EI}$, where P is the distributed load, L is the length, E is the elastic modulus, and I is the area moment of inertia. For a rectangular cross-section loaded in-plane, $I = \frac{hw^3}{12}$. Using these relations, we calculate that a straight cantilever beam with a $h:w$ ratio of 10:1 would exhibit 100 times more deflection in the in-plane direction than in the out-of-plane direction, assuming the same distributed load P in both loading directions. The relative out-of-plane deflection is anticipated to be even lower due to the in-plane actuation that induces a distributed load primarily in-plane.

We have also quantified the out-of-plane motion by measuring the displacement of the end of the flagellum in simulations for $\theta_0 = 90^\circ$. As shown in Figure S1, the end displacement is approximately three orders of magnitude lower than the height of the flagellum (5 mm), demonstrating that the flagellum motion was primarily in-plane.

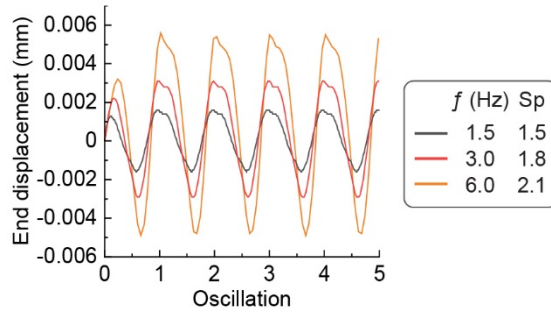


Figure S1: Out-of-plane displacement of the end of the flagellum in simulations for $\theta_0 = 90^\circ$.

B. Frequencies chosen for analysis

This study focuses on three frequencies ($f = 1.5, 3.0,$ and 6.0 Hz) based on the preliminary simulation results shown in Figure S2 for a flagellum with $\theta_0 = 90^\circ$. We primarily focus on relatively low frequencies to better understand the negative propulsion regime. We chose $f = 3.0$ Hz, as it was near the minimum $\langle Fp \rangle$. We chose $f = 6.0$ Hz, as the $\langle Fp \rangle$ was positive at approximately the same magnitude as the $\langle Fp \rangle$ at 3.0 Hz, and because 6.0 Hz was near the upper limit for the motor speed in the experimental setup. We chose $f = 1.5$ Hz as the lower bound due to hardware limitations in the experimental setup, as the motor would stall at lower speeds.

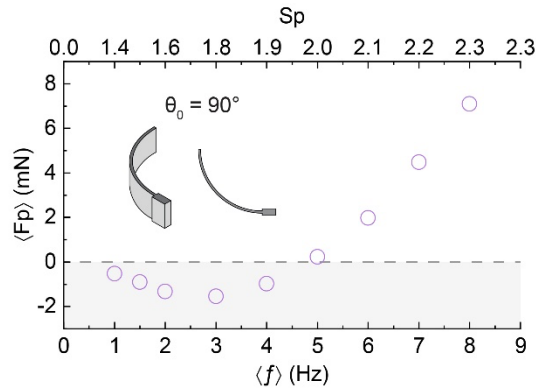


Figure S2: Time-averaged propulsive force over a range of frequencies for a flagellum with $\theta_0 = 90^\circ$. Data are from FE simulations. The top axis shows the non-dimensional Sp .

C. Macroscale experiment load cell information

Force data were acquired using a load cell (ANYLOAD 108AA-100g, Tacuna Systems) attached to the top of the actuation assembly. The load cell's datasheet reports the following specifications. Full scale output $1.0 \text{ mV/V} \pm 20\%$, non-linearity $< \pm 0.023\%$, repeatability $< \pm 0.023\%$, hysteresis error $< \pm 0.023\%$, creep in 30 min. $< \pm 0.050\%$.

D. Steady state

To determine the number of oscillations required to reach a steady state, we performed experiments with the flagellum having $\theta_0 = 90^\circ$ and calculated the average Fp for each oscillation. As shown in Figure S3, experiments at $\langle f \rangle = 6 \text{ Hz}$, 4 Hz , and 2 Hz reached a steady state before approximately oscillation 40. Based on these results, the experimental $\langle Fp \rangle$ and $\langle f \rangle$ were calculated using the respective data between oscillations 40 and 50.

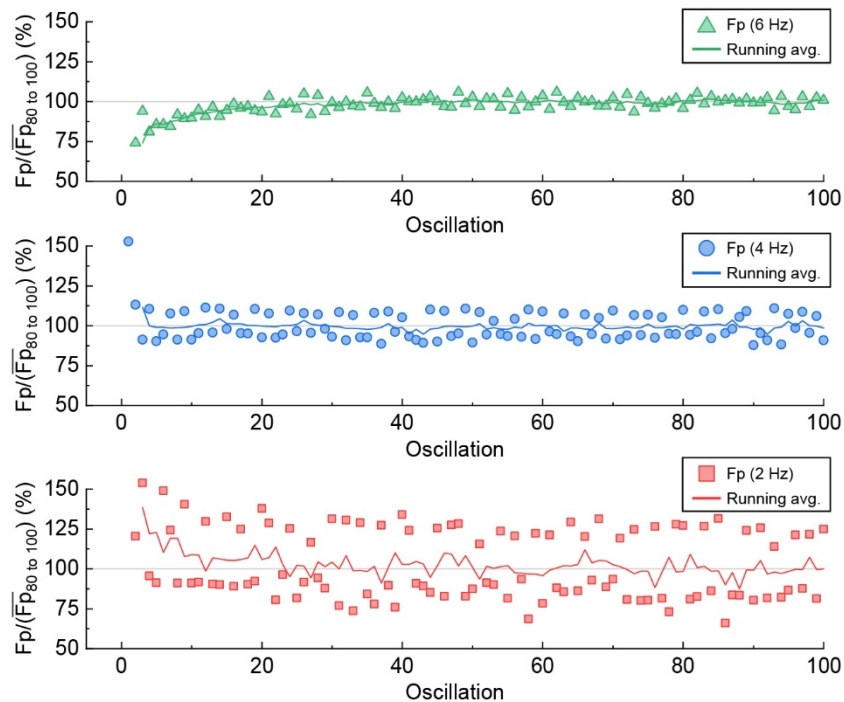


Figure S3: Experimental propulsive force of the flagellum with $\theta_0 = 90^\circ$ over 100 oscillations. Datapoints represent the average Fp in each oscillation for experiments at $\langle f \rangle = 6 \text{ Hz}$ (top), 4 Hz (middle), and 2 Hz (bottom). To enable visualization of the steady state, the Fp data are divided by the average Fp between oscillations 80 and 100. A running average (centered across 5 datapoints) is included in each plot.

E. Compensating for the no-flagellum force in the experimental Fp

As shown in Figure S4, the actuation assembly used in the macroscale experiments produces a non-zero propulsive force (grey data) during the transverse oscillation. This experimental “no-flagellum” force can be attributed to imperfect balancing in the actuation assembly and the motion of the slider (i.e., the segment that attaches to the clamped end of the flagellum) through the fluid during the transverse oscillation. To compensate for the no-flagellum force in the experimental results, we can subtract the experimental results by a fit to the no-flagellum data. A comparison between the plots in Figure S4 shows that the second-order polynomial fit to the no-flagellum data results in the corrected data being closer to zero across the measured f range (see blue data in Figure S4B).

In this study, we compensated for the no-flagellum force by subtracting Fp by the second-order polynomial fit to the no-flagellum data. For example, in Figure 2A in the main text, the experimental $\langle Fp \rangle$ are corrected using the following equation: $Fp_{corrected} = \overline{Fp} - (-0.098f^2 + 2.44f - 1.63)$. By way of comparison, Figure S5 shows the same experimental $\langle Fp \rangle$ without correcting for the no-flagellum force. A comparison between Figure 2A and Figure S3 demonstrates that correcting for the no-flagellum force results in experimental $\langle Fp \rangle$ that more closely agree with the simulation $\langle Fp \rangle$.

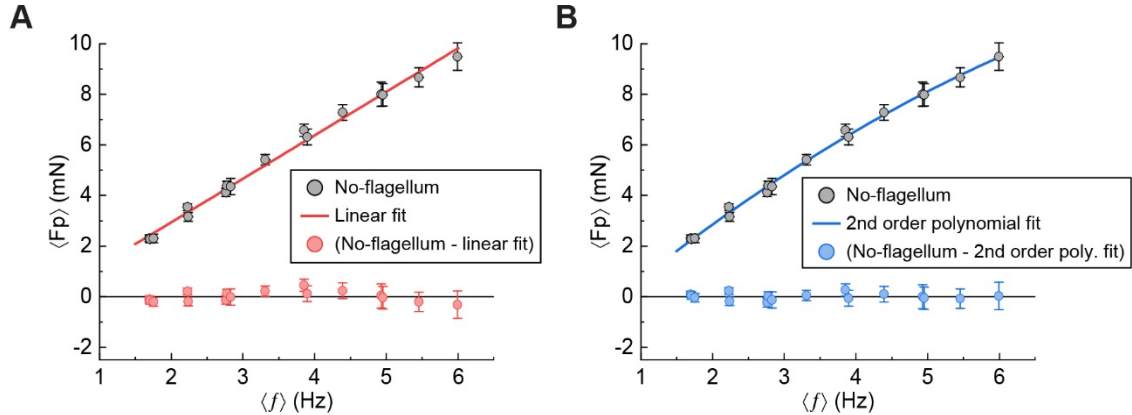


Figure S4: Compensating for the no-flagellum force. Time-averaged propulsive force (Fp) across a range of f from approximately 1.5 Hz to 6.0 Hz. Grey data show $\langle Fp \rangle$ for the actuation assembly with no flagellum attached (“no-flagellum”). In A, a linear fit is calculated from the no-flagellum data (red line, $y = 1.72x - 0.50$). In B, a second-order polynomial fit is calculated from the no-flagellum data (blue line, $y = -0.098x^2 + 2.44x - 1.63$). To compensate for the no-flagellum force in the experimental results, we can subtract the experimental results by the linear fit (shown in A) or by the second-order polynomial fit (shown in B). In both plots, the error represents the standard deviation across 10 oscillations at steady state.

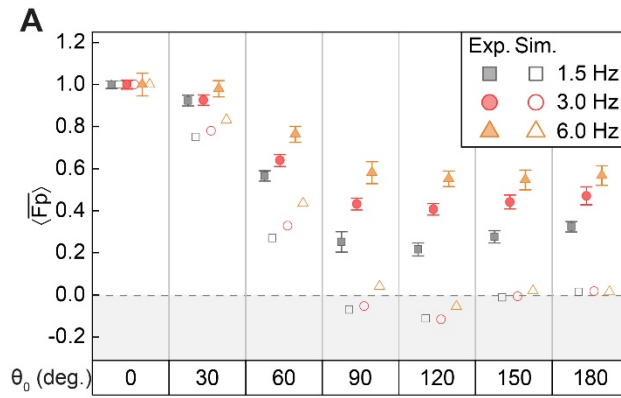


Figure S5: Curvature-dependent propulsion, where experimental data have not been corrected to account for the no-flagellum force. The plot shows normalized $\langle \hat{F}p \rangle$ as a function of θ and $\langle f \rangle$. All designs have the same dimensions ($L = 22$ mm, $h = 5$ mm, $w = 0.5$ mm) and were actuated at three frequencies ($f = 1.52 \pm 0.03$, 3.03 ± 0.01 , and 6.00 ± 0.03 Hz; error represents standard deviation across all experimental trials at each frequency) with $\beta = 0.25$. Experimental (solid) and simulation (open) data were acquired at each f and θ_0 , where experimental error bars represent the standard deviation across 20 oscillations at steady state (10 oscillations each for two experiments at each f). In the plot, the experimental data have not been corrected to account for the no-flagellum force.

F. Simulation mesh

The computational meshes were generated in COMSOL with a fine mesh setting. Sample simulation domains illustrating the mesh design (Figure S6) show a close-up of the flagella with surrounding fluids. We locally refined the mesh to ensure we captured the complete physics near the flagella.

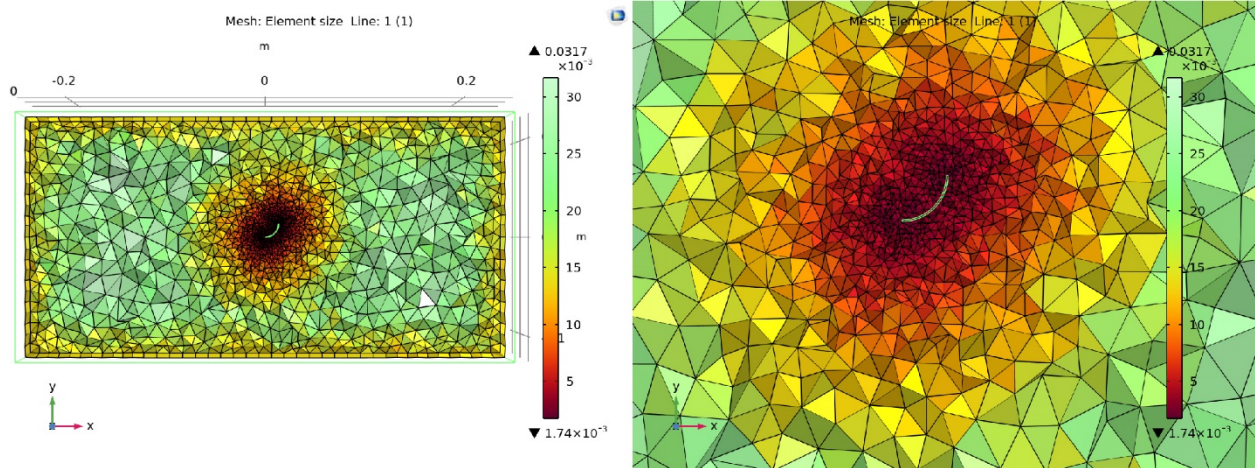


Figure S6: Sample simulation domains illustrating the mesh design. The images show a cross-sectional view at $z = 0$ for the three-dimensional mesh. The color represents mesh size, showing local refinement of the mesh around the flagella.

G. Differences in the geometrical setups between the experiments and simulations

To understand the effect of the different geometrical setups on Fp , we performed simulations with the flagellum having $\theta_0 = 90^\circ$ (chosen due to the differences between the experimental and simulation results). We included a rigid rectangular prism representing the slider (i.e., the orange-colored segment extending from the actuation assembly to the flagellum in Figure 1D) that is attached to the fixed end of the flagellum and moves with the actuation. The slider was critical to perform the transverse oscillation in the experimental setup, but was not included in the simulations performed for Figure 2A. We hypothesized that the slider could affect the Fp by changing the flow characteristics near the flagellum. Consequently, we performed simulations with and without the slider, where we used a smaller fluid volume to enable an even finer mesh size. A comparison of the $\langle Fp \rangle$ with and without the slider is shown in Figure S7.

A comparison of the results in Figure S7A shows that the slider increases $\langle Fp \rangle$ across the studied range of frequencies. This increase in Fp due to the slider may be an overprediction, as the slider in the simulation was a rectangular prism while the experimental slider had a diamond cross-section to reduce drag. On the other hand, imperfections in the experimental setup (e.g., clearance between parts, motor vibration) likely caused small vibrations in the experimental slider's motion that were not replicated in the simulation. The results in Figure S7A suggest that some of the differences between the experimental and simulation results can be attributed to differences in the geometrical setup from the slider.

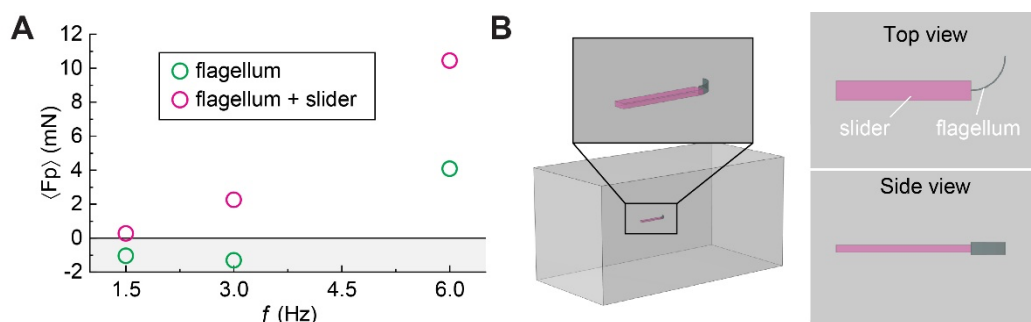


Figure S7: Effect of the slider on Fp . (A) Simulation results of $\langle Fp \rangle$ at $f = 1.5, 3.0,$ and 6.0 Hz for the flagellum (green data) and the flagellum + slider (pink data). (B) Images showing the slider (pink) attached to the flagellum (grey) with $\theta_0 = 90^\circ$.

H. Transition between positive and negative propulsion

To further investigate the transition between positive and negative propulsion, we performed additional simulations using flagella with $\theta_0 = 70^\circ$, 80° , and 85° . The results, shown in Figure S8, show that the transition between positive and negative propulsion occurs near $\theta_0 = 80^\circ$ at 1.5 Hz and near $\theta_0 = 85^\circ$ at 3.0 Hz.

The transition between positive and negative propulsion near $\theta_0 = 90^\circ$ can be understood by using a single-spring reduced-order model in previous work.¹ The model consists of two rigid rods of equal length, where rod 1 is clamped perpendicular to the transverse actuation and rod 2 is attached to rod 1 with a spring that is undeflected at an offset angle φ_I . Because the rods are rigid and rod 1 is at the same orientation throughout the oscillation, rod 1 does not exhibit any net propulsion. Consequently, the $\langle Fp \rangle$ depends entirely on rod 2. Using this model, the authors showed that $\langle Fp \rangle < 0$ when $\varphi_I > 45^\circ$, $\langle Fp \rangle = 0$ when $\varphi_I = 45^\circ$, and $\langle Fp \rangle > 0$ when $\varphi_I < 45^\circ$. The zero $\langle Fp \rangle$ at $\varphi_I = 45^\circ$ indicates that the time-varying Fp had positive and negative propulsion with equal magnitude. The negative $\langle Fp \rangle$ when $\varphi_I > 45^\circ$ indicates that the time-varying Fp had a larger magnitude of negative propulsion than positive propulsion during the oscillation.

We can use the previous reduced-order model to understand the transition between negative and positive propulsion in the present work by simplifying the intrinsically curved profile as a straight rigid rod. Specifically, we model the flagellum with uniform intrinsic curvature as a straight rod connecting the flagellum endpoints, where $\varphi_I = \theta_0/2$ due to geometric relations. Using this assumption, the model would predict negative propulsion when $\theta_0 > 90^\circ$ (as $\theta_0 = 2\varphi_I$), which is relatively close to the transition in the experimental and simulation results between $\theta_0 = 60^\circ$ and 90° . We anticipate that the transition point in the present work is lower than the $\theta_0 = 90^\circ$ prediction, as the curved flagellum can more easily decrease θ (i.e., straighten) than increase θ due to the increased length perpendicular to the transverse oscillation when traveling in the positive y -direction.

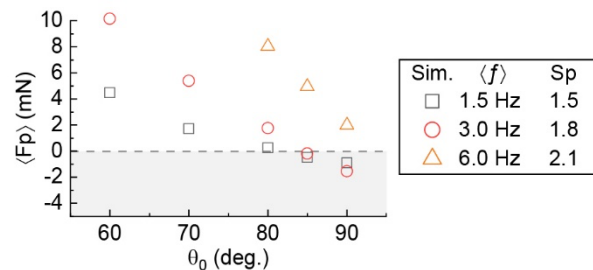


Figure S8: Simulation results of $\langle Fp \rangle$ for three frequencies (1.5, 3.0, and 6.0 Hz). The results show that the transition between positive and negative propulsion occurs near $\theta_0 = 80^\circ$ at 1.5 Hz and near $\theta_0 = 85^\circ$ at 3.0 Hz.

I. Full experimental results from Figure 2A

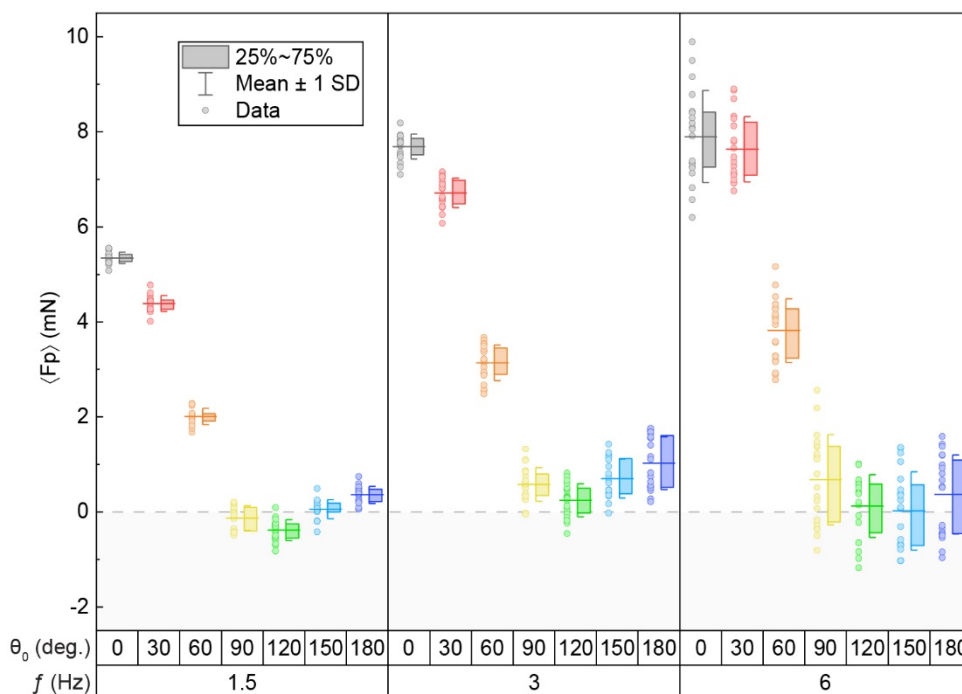


Figure S9: Detailed representation of the data in Figure 2A. The data points show the $\langle Fp \rangle$ across one oscillation, where there are 20 oscillations (2 tests, each with 10 oscillations) at steady state for each combination of f and θ_0 . The horizontal line through the data and box represents the mean, the box represents 25% to 75%, and the whiskers represent the mean \pm one standard deviation. The data for the experiment with $f = 1.5$ Hz and $\theta_0 = 120^\circ$ show that only one of the 20 oscillations had a mean propulsive force above zero, and that the standard deviation is entirely below zero. The results also show that increasing f tends to increase the standard deviation due to the increased amplitude of the time-varying Fp .

Our simulation and experimental results show that the $\langle Fp \rangle$ for the flagellum with $\theta_0 = 180^\circ$ is positive (see Figure 2A, Figure S9, and Figure S11), which means that the curvature-dependent $\langle Fp \rangle$ does indeed go through another sign reversal. We suspect that the positive force at $\theta_0 = 180^\circ$ could be due to fluid drag acting primarily on the convex surface of the semi-circular flagellum in both oscillation directions, whereas with designs having lower θ_0 , actuation in the positive y -direction causes fluid drag on the flagellum's concave surface. While future studies could investigate this finding further, the sign reversal and positive force at $\theta_0 = 180^\circ$ are unlikely to be useful in practical implementation, as the free end of a flagellum with $\theta_0 > 180^\circ$ would be past the driven end (in the positive x -direction). The relatively low $\langle Fp \rangle$ for the flagellum with $\theta_0 = 180^\circ$ is also likely due to the reduced length of the flagellum perpendicular to the oscillation direction (as this length exhibits the most drag-induced forces from the transverse actuation). Consequently, strategies for optimizing propulsion for configurations exhibiting both positive and negative strokes may need to account for the length of the flagellum that is perpendicular to the oscillation direction.

J. Propulsion at higher β

To investigate the effect of β on $\langle Fp \rangle$ in the present study, we performed experiments and simulations with $\beta = 0.5$ using the flagellum with $\theta_0 = 120^\circ$. We hypothesized that increasing β would increase $|\langle Fp \rangle|$, as previous literature reported that the propulsive force scales with β^2 .¹⁻⁵ We also hypothesized that increasing β would decrease the signal-to-noise ratio of the system by increasing the propulsive force relative to the noise from the experimental setup. The results of the experiments and simulations are shown in Figure S10.

The experimental results in Figure S10C and the simulation results in Figure S10F suggest that $|\langle Fp \rangle|$ scales with β^2 , which aligns with our hypothesis and is consistent with previous studies.¹⁻⁵ Interestingly, these results show the propulsive force scaling with β^2 despite the differences between the experimental and simulation results. As we have noted, we suspect that differences between the experimental and simulation results may be attributed to differences in the geometrical setup (e.g., from the slider that is used for the actuation in the experimental setup).

The experimental results in Figure S10C show that the experimental results for $\langle Fp \rangle/\beta^2$ had relatively smaller error bars with $\beta = 0.5$, which agrees with our hypothesis that the signal-to-noise ratio would increase with increasing β . A comparison between Figure S10B and Figure S10C shows that the improvement in the signal-to-noise ratio is due to the experimental error being comparable between the results with $\beta = 0.25$ and 0.5 , while the force magnitude increased with increasing β . Building upon this demonstration, future studies could similarly perform experiments at higher β to reduce the relative noise in the experimental setup (e.g., from the motor vibration).

We also note that the results in Figure S10D further show the negative propulsion at $f = 1.5$ Hz ($Sp = 1.5$) with the flagellum having $\theta_0 = 120^\circ$. In the plot, each datapoint represents the average propulsive force for one oscillation at steady state. All 30 datapoints (3 experiments with 10 oscillations each) are below zero, which aligns with the negative propulsion shown in Figure 2A.

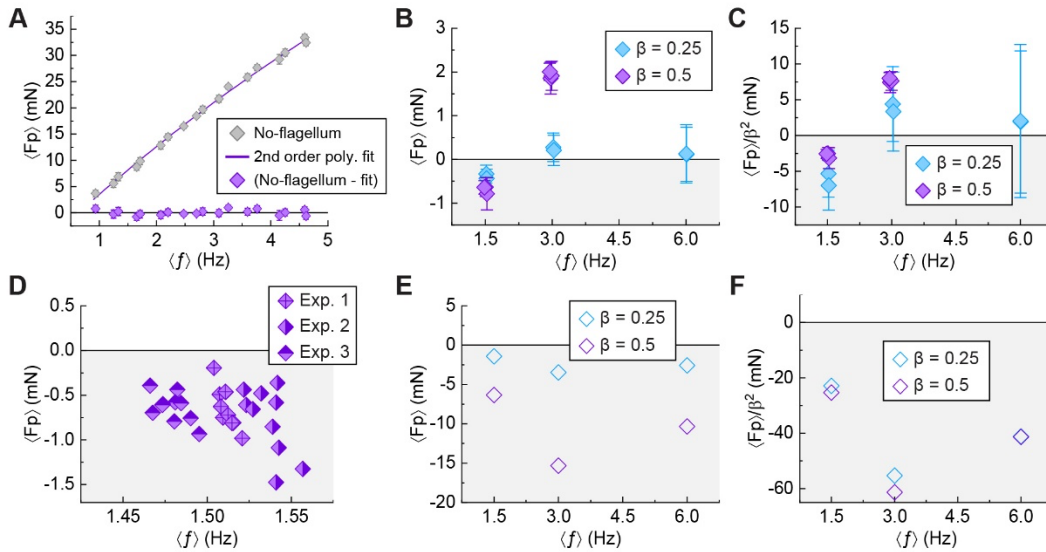


Figure S10: Experimental and simulation results for a flagellum with $\theta_0 = 120^\circ$ oscillated at $\beta = 0.25$ and $\beta = 0.5$. (A) Experimental time-averaged propulsive force $\langle Fp \rangle$ across a range of f from approximately 1 Hz to 5 Hz. Grey data show $\langle Fp \rangle$ for the actuation assembly with no flagellum attached (“no-flagellum”) when oscillated at $\beta = 0.5$. A second-order polynomial fit is calculated from the no-flagellum data (purple line, $y = -0.36x^2 + 10.18x - 6.31$). This fit was used to compensate for the no-flagellum force in the experimental results with $\beta = 0.5$. (B-C) Experimental $\langle Fp \rangle$ at $\beta = 0.25$ (blue data, taken from Figure 2A), and $\beta = 0.5$ (purple data), where the error bars represent the standard deviation across 10 oscillations at steady state. In C, the $\langle Fp \rangle$ is divided by β^2 . Experiments with $\beta = 0.5$ at $f = 6.0$ Hz were not performed due to the high translational velocity at $\beta = 0.5$ that caused the slider to break. (D) Fp for ten oscillations at steady state in three experiments at $\beta = 0.5$. (E-F) Simulation results for $\langle Fp \rangle$ at $\beta = 0.25$ (blue data, taken from Figure 2A), and $\beta = 0.5$ (purple data). In F, the $\langle Fp \rangle$ is divided by β^2 .

K. Sp-dependent propulsion

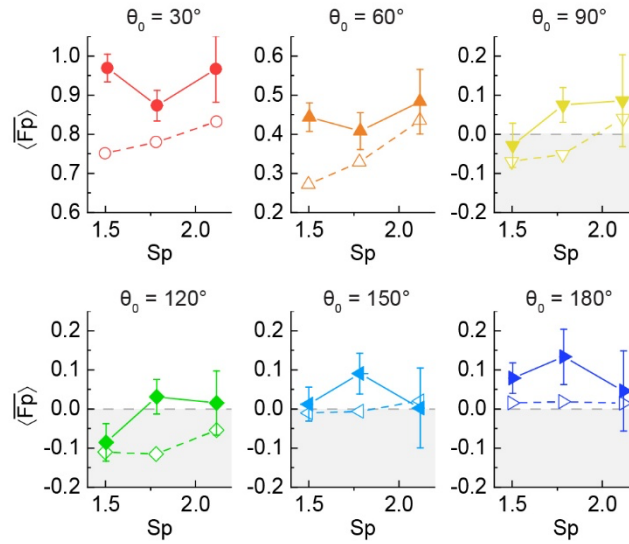


Figure S11: Effect of Sp and θ_0 on $\langle Fp \rangle$. The data are the same as shown in Figure 2A, here represented differently to better demonstrate the effect of Sp . Open datapoints represent simulation results, while filled datapoints represent the experimental mean with error bars representing one standard deviation. Lines connecting the datapoints (dashed: simulation, solid: experiment) are included to help guide the eye.

L. Comparison of the flagellum curvature

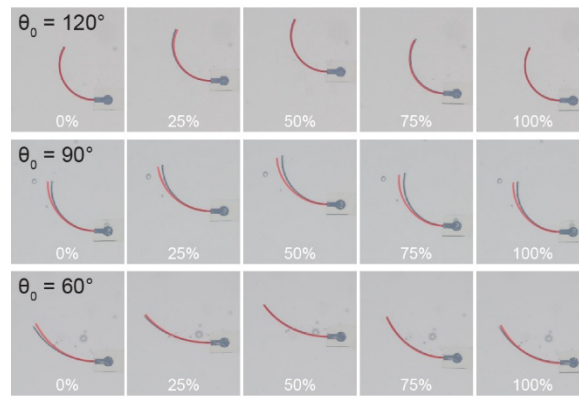


Figure S12: Comparison of flagellum curvature between experiments and simulations. Experimental images at approximately 0%, 25%, 50%, 75%, and 100% of an oscillation for flagella with $\theta_0 = 120^\circ$ (top row), 90° (middle row), and 60° (bottom row). To enable comparison with the simulations, the simulation profile is overlaid onto each image in red with 50% transparency.

II. ESI VIDEO CAPTIONS

ESI Video 1: Experimental video of the flagellum designed with $\theta_0 = 0^\circ$ at $\langle f \rangle \approx 1.5$ Hz. In the video, the flagellum is viewed from above, and the positive direction of Fp is to the right.

ESI Video 2: Experimental video of the flagellum designed with $\theta_0 = 30^\circ$ at $\langle f \rangle \approx 1.5$ Hz. In the video, the flagellum is viewed from above, and the positive direction of Fp is to the right.

ESI Video 3: Experimental video of the flagellum designed with $\theta_0 = 60^\circ$ at $\langle f \rangle \approx 1.5$ Hz. In the video, the flagellum is viewed from above, and the positive direction of Fp is to the right.

ESI Video 4: Experimental video of the flagellum designed with $\theta_0 = 90^\circ$ at $\langle f \rangle \approx 1.5$ Hz. In the video, the flagellum is viewed from above, and the positive direction of Fp is to the right.

ESI Video 5: Experimental video of the flagellum designed with $\theta_0 = 120^\circ$ at $\langle f \rangle \approx 1.5$ Hz. In the video, the flagellum is viewed from above, and the positive direction of Fp is to the right.

ESI Video 6: Experimental video of the flagellum designed with $\theta_0 = 150^\circ$ at $\langle f \rangle \approx 1.5$ Hz. In the video, the flagellum is viewed from above, and the positive direction of Fp is to the right.

ESI Video 7: Experimental video of the flagellum designed with $\theta_0 = 180^\circ$ at $\langle f \rangle \approx 1.5$ Hz. In the video, the flagellum is viewed from above, and the positive direction of Fp is to the right.

III. REFERENCES

- 1 Z. Liu, F. Qin and L. Zhu, *Phys. Rev. Fluids*, 2020, **5**, 124101.
- 2 E. Lauga, *Phys. Rev. E*, 2007, **75**, 041916.
- 3 Z. Liu, F. Qin, L. Zhu, R. Yang and X. Luo, *Phys. Fluids*, 2020, **32**, 041902.
- 4 C. H. Wiggins and R. E. Goldstein, *Phys. Rev. Lett.*, 1997, **80**, 3879–3882.
- 5 Z. Peng, G. J. Elfring and O. S. Pak, *Soft Matter*, 2017, **13**, 2339–2347.